Accepted Manuscript

Effect of coating weight on fiber laser welding of Galvanneal-coated 22MnB5 press hardening steel

M.H. Razmpoosh, A. Macwan, E. Biro, Y. Zhou

PII: S0257-8972(18)30061-6
DOI: https://doi.org/10.1016/j.surfcoat.2018.01.053
Reference: SCT 23036

To appear in: *Surface & Coatings Technology*

Received date: 6 October 2017
Revised date: 8 January 2018
Accepted date: 16 January 2018

Please cite this article as: M.H. Razmpoosh, A. Macwan, E. Biro, Y. Zhou , Effect of coating weight on fiber laser welding of Galvanneal-coated 22MnB5 press hardening steel. The address for the corresponding author was captured as affiliation for all authors. Please check if appropriate. Sct(2017), https://doi.org/10.1016/j.surfcoat.2018.01.053

Effect of Coating Weight on Fiber Laser Welding of Galvanneal-Coated 22MnB5 Press Hardening Steel

M.H. Razmpoosh[*a], A. Macwan[b], E. Biro[b], Y. Zhou[a]

[a]*Centre for Advanced Materials Joining, Department of Mechanical & Mechatronics Engineering, University of Waterloo, 200 University Avenue West, Waterloo, ON N2L 3G1, Canada*

[b]*ArcelorMittal Global Research, 1390 Burlington Street east, Hamilton, ON L8N 3J5, Canada*

Abstract

Tensile strengths of up to 1.5 GPa and fracture elongation of 8% in press-hardening steel (PHS) opened up a great opportunity to improve the crash performance of vehicles. However, due to the increased susceptibility to welding defects and undesired transformation as a result of coating mixing into the weld pool, laser welding of PHS is still challenging. Hence, the present study focuses on the effect of Galvanneal (GA)-coating weight on the microstructure and mechanical performance of fiber laser welded PHS. It was observed that GA-coating weight considerably affects the laser welding process window as well as weld geometry. Weld penetration decreased and concavity increased with increasing coating weight, which is attributed to intensified Zn-plasma and laser interaction at higher coating weights. Moreover, a model has been developed to interpret the correlation between the GA-coating weight of the PHS and the penetration depth based on the heat input per unit thickness of the sheet. The size of fusion zone and heat affected zone decreased slightly with increasing coating weight due to lower energy absorption by the material. Furthermore, GA-coating weight did not affect the tensile strength of all welded joints as the failure happened in the base metal.

Keywords: Fiber laser welding; Press-hardening steel; Galvanneal coating; Tensile strength; Microhardness.

[*] Corresponding author

Tel.: +12269783045

E-mail address: mhrazmpoosh@uwaterloo.ca (M.H. Razmpoosh)

1. Introduction

In the last decade, a significant research effort has been devoted to produce lightweight structural car components without sacrificing crashworthiness to achieve a reduction in the fuel consumption and greenhouse gas emissions (CO_2, CO, NOx). Hence, the automotive/steel-making industries are developing advanced high strength and ultra-high strength steel grades as well as novel manufacturing processes to address these vital demands [1–3]. Of particular interest is press-hardening steel (PHS) due to several technological advantages: Extremely high strength, good formability due to reduced flow stress during elevated temperature processing, minimum spring-back effect, and high dimensional accuracy [4,5]. Therefore, PHS has potential applications for several chassis components such as A-pillars, B-pillars, bumpers, roof rails, rocker rails, and tunnels.

It has been reported that during processing (austenitization/transferring stages), excessive oxidation and decarburization occurs [6–8]. Hence, various protective coating such as Al-Si, Zn-based, or Zn-Ni alloys has been developed and applied to protect the steel substrate against decarburization and scale formation [9–11]. Particularly, the aluminized and the Zn-based coating types attracted more attention [11]. It is well accepted that a 20–30 μm-thick aluminized coating of an Al-Si alloy with near-eutectic composition (7–11 wt% Si) has an excellent resistance to corrosion and elevated temperature scale formation [12]. Alternatively, Zn-based coatings fall into two main types: galvanized (GI) and galvanneal (GA). The GI-coating consists of a layer of elemental Zn on the surface of the steel; however, the GA type has a significant amount of Fe as a result of Fe-Zn inter-diffusion due to the post-dip annealing stage at temperatures of about 480°C.

The successful implementation of these steel and coating systems depend on their ability to be welded during manufacturing. Laser welded blanks (LWBs), in particular, have become commonplace in automotive manufacturing, enabling design engineers to use ultra-high strength materials in critical locations without sacrificing the overall flexibility and the dimensional accuracy [13]. LWBs are made from two or more similar and dissimilar sheets with different thicknesses which are formed into automotive parts. Recently, fiber laser welding (FLW) has gained popularity due to its small beam diameter, lower thermal distortion and residual stresses, high welding speed, and reduced manufacturing costs [14–16]. In past decades, extensive studies have been carried out on laser beam welding of AHSS including ultra-high strength steels such as PHS [17–20]. Recent studies have shown laser welding of Al-Si coated PHS pose a significant challenge. It was reported that the FLW of Al-Si-coated PHS lead to substantial Al mixing in the FZ resulting into the formation of a continuous structure of δ-ferrite through shrinking the single-phase austenite region (as Al is a strong ferrite stabilizer) [17,21]. This has a large effect on the tensile behavior of the joint and results in a drastic reduction in ductility after hot-stamping the joint. For example, Kim *et al.* [19] reported that FLW of Al-Si coated hot-stamping steel in lap configuration resulted in the formation of Fe-Al intermetallic compounds along the fusion line, resulting in the failure along the fusion boundary during the tensile shear test. Lee *et al.* [19] also studied the Nd: YAG laser lap joining behavior of Al-coated carbon steel and observed the deleterious effect of brittle intermetallic compounds on the strength of the joint.

Zn-based coatings due to their durability, cost-effectiveness and strong corrosion resistance are considered as the main protective coatings on a wide range of automotive-compatible steels [22–24]. Therefore, Zn-based coatings are considered as a viable alternative for PHS due to their ability to be welded without affecting fusion zone structure [25–28]. According

to Akhter et al. [29], Zn-coating affects laser stability during welding as a result of the well-known explosive vaporization of Zn. However, a limited research work dedicated to the effects of Zn-coating on laser welding of PHS in the present literature. Hence, as a starting point to investigate the effect of Zn-coatings on laser weldability of PHS, the present study focuses on characteristics and properties of FLW joints of GA-coated PHS sheets and analyzes effects of coating weight within the manufacturer's specification on the laser welding process.

2. Material and Experimental Procedure

In the present study, 2 mm-thick sheets of 22MnB5 steel holding three different thicknesses of GA-coatings were used. A summary of the major alloying elements and mechanical properties of the provided base material (BM) and detailed coating specification are given in Table 1 and 2, respectively. The yield strength (YS), the ultimate tensile strength (UTS) and total elongation (El) of the experimental material were 415 MPa, 590 MPa, and 14%, respectively. The provided steel sheets were mechanically sheared into 100 mm×200 mm coupons. The edges of the workpieces were milled and then clamped properly utilizing a designed system of fixtures to maintain alignment as well as to minimize distortion during the welding process. Accordingly, 200 mm×200 mm TWBs were produced in the butt-joint configuration using an IPG Photonics Ytterbium (YLS-6000-S2) fiber laser system equipped with a Panasonic robotic arm. The fiber core diameter, the spot size, and the beam focal length were 0.3, 0.6 and 200mm, respectively. The welding trials were performed perpendicular to the rolling direction, holding a head angle of 25° where no shielding gas was used during the process, however, the high-pressure air was applied to push vapors far from the weld pool, and

simultaneously providing a protection for the laser system optics. Laser welding trials were carried out under a range of 3 to 6 kW welding power at increments of 1 kW and 8 to 22 m/min of welding speed with an increment of 4 m/min.

In order to investigate the microstructural evolution, through-thickness cross-sections were cut from the welded material. The conventional preparation procedure including mounting, grinding, polishing to 1μm and etching was followed. The etched samples were observed across the welded region, by means of optical and Zeiss Leo 1530 field emission scanning electron microscopy (FESEM), equipped with energy dispersive X-ray spectroscopy (EDS). The coating was characterized in detail by means of electron probe micro analysis (EPMA) and X-Ray diffraction (XRD). Vickers microhardness profiles across the welded region were obtained using a load of 300 g and a dwell time of 15 s. All the reported values were an average of three series of values recorded. In addition, the indentations were applied sufficiently far from each other to avoid any undesired interference from the localized strain hardening from the adjacent ones.

Sub-sized tensile specimens were machined from the provided TWBs according to ASTM: E8/E8M. The welded samples were machined perpendicular to the welding direction, where, the laser weld line located at the center of the gauge length. Fig. 1 represents the geometry of the tensile coupons used in the present study. Furthermore, the gauge area of the provided test specimens was ground by means of sandpapers up to 1200 grit. Tensile trials were carried out utilizing a fully-computerized universal testing machine at ambient temperature and strain rate of 1×10^{-3} s^{-1} until their rupture. At each tensile condition, at least three samples were tested separately. Moreover, the fracture surfaces of tensile specimens were investigated by SEM.

3. Results and discussion

3.1. As-received base material and coating characteristics

The steel substrate contained a ferrite matrix (average grain size of about 10μm) decorated with dispersed colonies of pearlite structure as shown in Fig. 2(a). Fig. 2(b-d) shows the cross-section SEM image and corresponding EPMA elemental distribution and phase mapping of the GA-coating on the steel substrate. By means of EPMA elemental distribution and phase map (based on the both Fe-Zn intermetallic phases' Zn content ranges and BSE-SEM image processing), two main layers inside the coating can be distinguished. As proven by XRD analysis (Fig. 2(e)), the coating mainly consisted of Γ-Fe_3Zn_{10}, Γ1- Fe_5Zn_{21} and δ-$FeZn_{10}$ phases. Therefore, based on the XRD and EPMA elemental/phase map results in Fig. 2(d), Γ/Γ1 and δ phase can be assigned to green (~1-2μm in thickness) and red (~7μm in thickness) regions, respectively. The presence of Γ/Γ1 and δ phases in the coating is in agreement with previous research works, where the (Γ/Γ1) and δ layers possess about 75 and 90 wt% of Zn, respectively [30].

3.2. Microstructure of the weld

Fig. 3 shows overall microstructure showing various zones (BM, Inter-Critical heat affected zone (ICHAZ), Upper-Critical heat affected zone (UCHAZ), and Fusion Zone (FZ) for sample welded at the power of 4 kW and a welding speed of 8 m/min of with a coating weight of 140 g/m^2. Coating condition did not affect the welded microstructure, as the different regions appeared similar in various coating conditions. According to Fig. 3(a), and as noted previously, the BM comprised of ferrite grains decorated with pearlite colonies. However, the ICHAZ

consisted of ferrite grains, pearlite, and martensite (Fig. 3(b) and (c)), whereas the peak temperature during the heating cycle of the welding process in this region reached as high as temperatures between the Ac_1 and Ac_3 of the experimental steel, where ferrite and austenite coexists. As observed in Fig. 3(d), within the ICHAZ, martensite mainly formed on the grain boundaries of ferrite as well as at interface of pearlite colonies and ferrite. This was mainly attributed to the fact that during the heating cycle of the welding process, austenite nucleated on the ferrite grain boundaries i.e. incomplete austenitization started from the grain boundaries. According to Saha *et al.* [31], the cooling rate in the heat affected zone (HAZ) of the fiber laser welded samples could be approximated using the Rosenthal Eq. [32]. In this regard, the cooling rate (CR) would exceed the 10^4 °C/s. It is well-reported by various authors, the critical CR for the experimental steel to achieve a full martensitic transformation from austenite is around 27 °C/s [5]. Moreover, within the UCHAZ (Fig. 3(e)), the peak temperature exceeds the critical Ac_3 temperature and as a net consequence, austenitic structure fully transforms into martensite. It should be noted that with respect to increasing peak temperature with decreasing the distance to the weld centerline, the martensite volume fraction increases. As pointed out, this is attributed to increasing volume fraction of austenite from Ac_1 to Ac_3 in the ICHAZ. Since, the CR is well higher than the critical rate within the HAZ, it is expected that all the emerged austenite retransform into martensite. As seen in Fig. 3(a), (f) and (g), a typical full martensitic microstructure was attained in the FZ. As reported by past works [33,34], two different kinds of lath martensite would develop during rapid martensitic transformation. Fig. 3(f) shows the presence of the coarse lathes (red arrows) as well as finer lathes. There is a slight difference in the appearance of coarse and fine lathes in the FZ, where coarser lathes possess relatively tempered appearance. As reported [33] the coarse lathes form at early stages of transformation,

where the temperature is relatively high below M_s temperature. Therefore, these coarse lathes are more prone to be auto-tempered compared to those of finer counterparts (Fig. 3(g)) formed at a later stage [33].

In order to investigate whether the GA coating influenced the weld pool, EDX analysis was done within the FZ. EDX analysis detected the presence of Zn with an average of 0.68 wt% within the indicated location of the FZ (Fig. 4). A significant Al-coating mixing into the weld pool and presence of ~2.5wt% Al in ferrite phase has been reported previously by Saha *et al*. [21] in the course of FLW of PHS. As is delineated by Saha *et al*. [17,21], one may expect a severe coating mixing into the FZ based on the well-established keyhole formation concept in terms of FLW. However, due to the much lower boiling point of Zn-based coating, Zn mainly evaporates during the process. That justifies very low content of Zn in the FZ.

3.3. Effect of the coating weight on welding behavior

In order to investigate the effects of the various coating weight on FLW parameter window, bead-on-plate (BoP) welds were made using the aforementioned welding parameters. Accordingly, Fig. 5 represents the process map in various coating conditions, using the GM4485M acceptance criteria [35] of concavity, convexity and penetration depth (d) in a wide range of welding power and speed combinations. According to GM4485M, in a full-penetrated weld, convexity lower than 10% of sheet thickness (t) and concavity lower than 20% of t falls within the acceptable joint. On this basis, two boundaries of the convexity over the acceptance limit of 10% of original thickness as well as full penetration holding acceptable concavity on top were defined. It was observed that with increasing coating weight, the region of acceptable joint region shifts toward higher laser powers and lower welding speeds. Although in lower coating

weight (100 g/m^2), the process window is wider, the convexity over the acceptance which (appeared as a darker area) is relatively larger than higher coating weight (140 g/m^2) which reduces the overall acceptable region. Furthermore, increasing the coating weight from 100 to 140g/m^2, the overall acceptable region would shift toward higher welding power and lower welding speed. Moreover, it has been observed that size of the welding window slightly reduces with increasing the coating weight. The observed behavior could be attributed to plasma formation during laser welding of Zn-coated material. The boiling temperature of Zn is around 900°C, which is much lower than Fe. In addition, it was shown that vapor pressure of Zn is extensively higher than Fe. As reported by Chen *et al.* [36] the interaction between the laser and plasma is substantially affected by the Zn plasma. Therefore, one may expect that higher coating weight by intensifying ionized plasma negatively affect energy deliverance and subsequently reduces the penetration. In fact, at elevated temperatures, a higher electron density of Zn (two orders of magnitude greater than Fe) causes energy dissipation by plasma-beam interference [36]. This explains the growth of incomplete penetration zone and shrinkage of the over-convexity zone (Fig. 5(b) and (c)). As is well-established, the over convexity would occur as a result of excess heat input in terms of laser welding [37]. To shed light on the correlation between the penetration depth (d) and welding parameters, heat input per unit thickness (thickness-normalized heat input [38]) of the material was calculated based on the experimental results and relationship with penetration depth was established, as shown in Fig. 6. According to the Fig. 6, a model was developed to interpret the aforementioned correlation. This overall model could be used to estimate the penetration depth in various welding power/speed combinations at the various GA-coating weight (Eq. (1)):

$$\boldsymbol{d = (H - 8.6 + 0.08C)/(0.09C - 4.8)} \quad (1)$$

where d corresponds to the penetration depth (mm) and H is heat input per unit thickness (J/mm^2) and C is the coating weight (g/m^2). Based on the proposed model, one may predict the penetration depth in each GA-coating condition of the experimental material. The observed behavior is consistent with the previous work conducted on laser beam welding of steels [39].

3.4. Mechanical Properties

3.4.1 Microhardness

The microhardness profiles for different coating weight are compared in Fig. 7. It was observed that at the identical combination of welding power and speed, the width of the HAZ and the FZ is slightly dependent on the coating weight. As seen, with increasing the coating weight, the width of the HAZ, FZ, and consequently the overall weld width decreased slightly. This may be ascribed to the higher heat input delivered to the material with decreasing coating weight, which agrees with the earlier observation on the welding window. Moreover, in all coating conditions, the HAZ reveals the hardness magnitudes between the BM and the FZ, in agreement with the microstructural observations (Fig. 3 (b-d)). This could be attributed to the incremental volume fraction of the martensite with decreasing the distance from the weld centerline. As pointed out, increased martensite fraction was attributed to the retransformation of austenite within ICHAZ and UCHAZ into martensite in the course of cooling cycle. Despite the reported literature on the laser beam welding of AHSSs, the softening in the sub-critical HAZ (SCHAZ) of the experimental material is not expected. Various AHSSs show decomposition of the martensite in the BM to the partially tempered martensite (PTM) within the SCHAZ; however, due to the absence of the martensite in the as-received condition of the experimental steel, one may not expect the SCHAZ softening in this study.

3.4.2 Tensile behavior and failure analysis

Fig. 8 (a) shows the engineering stress vs. strain curves of the BM (with a coating weight of 140 g/m^2) and the provided joints at different coating conditions. The yield strength (YS), the ultimate tensile strength (UTS) and elongation to fracture (El) of the BM in different coating conditions were observed to be close together, and therefore the condition of 140 g/m^2 selected as the representative of mechanical properties of the BM. Significant necking was observed before failure in the BM area of the welded samples, which indicated strain localization was absent in the weld region. In other words, it was confirmed that concavity within the acceptance limit may not impose any detrimental effect on tensile behavior and joint efficiency is close to 100% According to Fig. 8 (b), no direct correlation between different coating conditions and YS, UTS and elongation to fracture levels was observed for welded samples i.e. the weld material is resistant to the various concavity levels irrespective of coating conditions. This was mainly attributed to the failure location in the BM, regardless of the coating condition. Therefore, one may not expect different tensile behavior at various coating weight. Fig. 7 (c) and (d) reveal the representative SEM micrographs of the fracture surface of the tensile specimens which showed typical ductile dimple morphology. The fracture surface characteristics were essentially analogous to various coating conditions holding an almost similar dimple sizes, where central fracture area revealed equiaxed dimples. In contrast, the fracture surface near the edge area (Fig. 7 (d)) demonstrated a shear fracture mode in addition to the typical ductile dimple morphology, which in turn confirms the incidence of shearing as well as tension in terms of the rupture.

4. Conclusions

Considering the effect of various GA-coating weight, the microstructure evolution and the mechanical response of fiber laser-welded press-hardening steel were investigated. The major findings of the present study are summarized as below:

(a) The microstructure of the FZ consisted of a typical lath martensitic structure with a combination of coarse and fine lathes due to the extreme high rate of cooling resulted in a significant increase in the hardness. Moreover, EDX analysis confirmed a slight mixing of the GA-coating into the weld pool.

(b) The welding window is dependent on the GA-coating weight, where by increasing coating weight, the welding window tends to be narrower and shifted toward higher laser power and lower welding speeds. This was mainly attributed to laser-Zn plasma interaction at higher coating weights resulting in higher energy dissipation. Accordingly, a model has been established to interpret the correlation between the heat input per unit thickness (combination of any welding power/speed) and penetration depth including a coating weight coefficient.

(c) The ultimate tensile strength (UTS) and elongation to fracture (El) remained almost unchanged after laser welding, showing a joint efficiency of 100%. A significant necking occurred before failure, which, in turn, suggests that the weld material is resistant to the various concavity levels in different coating conditions.

Acknowledgements

Authors would like to acknowledge the National Science and Engineering Research Council (NSERC) of Canada and ArcelorMittal Dofasco Inc. in Hamilton, Canada for providing the financial support and materials to carry out this work.

References

[1] L. Mujica Roncery, S. Weber, W. Theisen, Welding of twinning-induced plasticity steels, Scr. Mater. 66 (2012) 997–1001.

[2] M. Ghosh, K. Kumar, R.S. Mishra, Friction stir lap welded advanced high strength steels: Microstructure and mechanical properties, Mater. Sci. Eng. A. 528 (2011) 8111–8119.

[3] M.H. Razmpoosh, M. Shamanian, M. Esmailzadeh, The microstructural evolution and mechanical properties of resistance spot welded Fe–31Mn–3Al–3Si TWIP steel, Mater. Des. 67 (2015) 571–576.

[4] M. Abbasi, M. Naderi, A. Saeed-Akbari, Isothermal versus non-isothermal hot compression process: A comparative study on phase transformations and structure-property relationships, Mater. Des. 45 (2013) 1–5.

[5] H. Karbasian, A.E. Tekkaya, A review on hot stamping, J. Mater. Process. Technol. 210 (2010) 2103–2118.

[6] T.J. Yoon, M.H. Oh, H. jeong Shin, C.Y. Kang, Comparison of microstructure and phase transformation of laser-welded joints in Al-10wt%Si-coated boron steel before and after

hot stamping, Mater. Charact. 128 (2017) 195–202.

[7] K. Mori, D. Ito, Prevention of oxidation in hot stamping of quenchable steel sheet by oxidation preventive oil, CIRP Ann. - Manuf. Technol. 58 (2009) 267–270.

[8] M. Merklein, M. Wieland, M. Lechner, S. Bruschi, A. Ghiotti, Hot stamping of boron steel sheets with tailored properties: A review, J. Mater. Process. Technol. 228 (2016) 11–24.

[9] K. Uda, A. Azushima, A. Yanagida, Development of new lubricants for hot stamping of Al-coated 22MnB5 steel, J. Mater. Process. Technol. 228 (2016) 112–116.

[10] Z.X. Gui, W.K. Liang, Y.S. Zhang, Formability of aluminum-silicon coated boron steel in hot stamping process, Trans. Nonferrous Met. Soc. China (English Ed. 24 (2014) 1750–1757.

[11] D.W. Fan, B.C. De Cooman, State-of-the-knowledge on coating systems for hot stamped parts, Steel Res. Int. 83 (2012) 412–433.

[12] O.L. Ighodaro, E. Biro, Y.N. Zhou, Comparative effects of Al-Si and galvannealed coatings on the properties of resistance spot welded hot stamping steel joints, J. Mater. Process. Technol. 236 (2016) 64–72.

[13] M. Merklein, M. Johannes, M. Lechner, A. Kuppert, A review on tailored blanks - Production, applications and evaluation, J. Mater. Process. Technol. 214 (2014) 151–164.

[14] W. Xu, D. Westerbaan, S.S. Nayak, D.L. Chen, F. Goodwin, E. Biro, Y. Zhou, Microstructure and fatigue performance of single and multiple linear fiber laser welded DP980 dual-phase steel, Mater. Sci. Eng. A. 553 (2012) 51–58.

[15] D. Parkes, W. Xu, D. Westerbaan, S.S. Nayak, Y. Zhou, F. Goodwin, S. Bhole, D.L. Chen, Microstructure and fatigue properties of fiber laser welded dissimilar joints between high strength low alloy and dual-phase steels, Mater. Des. 51 (2013) 665–675.

[16] D. Parkes, D. Westerbaan, S.S. Nayak, Y. Zhou, F. Goodwin, S. Bhole, D.L. Chen, Tensile properties of fiber laser welded joints of high strength low alloy and dual-phase steels at warm and low temperatures, Mater. Des. 56 (2014) 193–199.

[17] D.C. Saha, E. Biro, A.P. Gerlich, N.Y. Zhou, Fusion zone microstructure evolution of fiber laser welded press-hardened steels, Scr. Mater. 121 (2016) 18–22.

[18] A.P.G. D.C. Saha, E. Biro, Fiber Laser Welding of Al-Si-Coated Press- Hardened Steel, Weld. J. 95 (2016) 147–156.

[19] C. Kim, M.J. Kang, Y.D. Park, Laser welding of Al-Si coated hot stamping steel, Procedia Eng. 10 (2011) 2226–2231.

[20] D.C. Saha, D. Westerbaan, S.S. Nayak, E. Biro, A.P. Gerlich, Y. Zhou, Microstructure-properties correlation in fiber laser welding of dual-phase and HSLA steels, Mater. Sci. Eng. A. 607 (2014) 445–453.

[21] D.C. Saha, E. Biro, A.P. Gerlich, Y.N. Zhou, Fiber Laser Welding of AlSi Coated Press Hardened Steel, Weld. J. 95 (2016) 147–156.

[22] N.T. Bandyopadhyay, G. Jha, A.K. Singh, T.K. Rout, N. Rani, Corrosion behaviour of galvannealed steel sheet, Surf. Coat. Technol. 200 (2006) 4312–4319.

[23] S. Ganesan, G. Prabhu, B.N. Popov, Surface & Coatings Technology Electrodeposition and characterization of Zn - Mn coatings for corrosion protection, Surf. Coat. Technol.

238 (2014) 143–151.

[24] S. Das, M. Dutta, N. Bandyopadhyay, N. Rajesh, Improvement in galvannealed coating of IF-HS steel strips by combined GDOES and colour-etching method, Surf. Coat. Technol. 201 (2007) 4547–4552.

[25] J. Kondratiuk, P. Kuhn, E. Labrenz, C. Bischoff, Surface & Coatings Technology Zinc coatings for hot sheet metal forming : Comparison of phase evolution and microstructure during heat treatment, Surf. Coat. Technol. 205 (2011) 4141–4153.

[26] C. Ji, I. Jo, H. Lee, I. Choi, Y. Kim, Y. Park, Effects of surface coating on weld growth of resistance spot-welded hot-stamped boron steels, J. Mech. Sci. Technol. 28 (2014) 4761–4769.

[27] C. Wook, W. Seok, Y. Rae, B.C. De Cooman, Surface & Coatings Technology Microstructure evolution of a 55 wt .% Al – Zn coating on press hardening steel during rapid heating, Surf. Coat. Technol. 281 (2015) 35–43.

[28] H. Yang, S. Zhang, J. Li, X. Liu, H. Wang, Surface & Coatings Technology Effect of strip entry temperature on the formation of interfacial layer during hot-dip galvanizing of press-hardened steel, Surf. Coat. Technol. 240 (2014) 269–274.

[29] R. Akhter, W.M. Steen, D. Cruciani, Proc. 5th Int. Conf. Lasers in Manufacturing, 195-206 September 1988,© IFS Ltd and authors, ISBN 1-85423-021-2, in: Lasers Manuf. Proc. 5th Int. Conf. 13-14 Sept. 1988, Stuttgart, West Ger., Springer Verlag, 1988: p. 195.

[30] A.R. Marder, Metallurgy of zinc-coated steel, Prog. Mater. Sci. 45 (2000) 191–271.

[31] D.C. Saha, E. Biro, A.P. Gerlich, Y. Zhou, Effects of tempering mode on the structural

changes of martensite, Mater. Sci. Eng. A. 673 (2016) 467–475.

[32] D. Rosenthal, The Theory of Moving Sources of Heat and Its Application of Metal Treatments, Trans. ASME. 68 (1946) 849–866.

[33] L. Morsdorf, C.C. Tasan, D. Ponge, D. Raabe, 3D structural and atomic-scale analysis of lath martensite: Effect of the transformation sequence, Acta Mater. 95 (2015) 366–377.

[34] B.B. He, M.X. Huang, Revealing the Intrinsic Nanohardness of Lath Martensite in Low Carbon Steel, Metall. Mater. Trans. A Phys. Metall. Mater. Sci. 46 (2014) 688–694.

[35] General Motors Engineering Standards, Weld Specifications Laser Welds-Butt Joints GM4485M, 2002.

[36] W. Chen, P. Ackerson, P. Molian, CO2 laser welding of galvanized steel sheets using vent holes, Mater. Des. 30 (2009) 245–251.

[37] D. Westerbaan, D. Parkes, S.S. Nayak, D.L. Chen, E. Biro, F. Goodwin, Y. Zhou, Effects of concavity on tensile and fatigue properties in fibre laser welding of automotive steels, Sci. Technol. Weld. Join. 19 (2014) 60–68.

[38] M. Xia, E. Biro, Z. Tian, Y.N. Zhou, Effects of Heat Input and Martensite on HAZ Softening in Laser, 48 (2008) 809–814.

[39] S. Miller, E. Pfeif, A. Kazakov, E. Baumann, M. Dowell, Fiber laser welding of dual-phase galvanized sheet steel (DP590): traditional analysis and new quality assessment techniques, High-Power Laser Mater. Process. Lasers, Beam Deliv. Diagnostics, Appl. V. 9741 (2016) 97410I.

Figure captions

Fig. 1. Schematic illustrations of the tensile test specimen machined from the FLW workpiece.

Fig. 2. (a) Representative microstructure of the as-received material, cross-sectional (b) SEM micrograph, (c) EPMA Zn distribution map, (d) phase map and (e) XRD phase identification of the Zn-coating (P: pearlite, F: ferrite).

Fig. 3. The microstructure of the weld material welded at 4kW and 8 m/min with coating weight of 140 g/m^2: (a) overall view, (b) HAZ, (c) ICHAZ at low and (d) high magnifications, (e) UCHAZ (f) FZ, and (g) coarse-lath martensitic structure (where M; martensite, P: pearlite, F: ferrite).

Fig. 4. Micrograph showing the location of EDS within the FZ.

Fig. 5. Process map of the welding window at coating weight of (a) 100 g/m^2, (b) 120 g/m^2, and (c) 140 g/m^2.

Fig. 6. The correlation between the heat input per unit thickness and penetration depth of FLW.

Fig. 7. A comparison of hardness profile of weld material made at 100, 120, and 140g/m^2 (at constant power of 4kW and welding speed of 8 m/min)

Fig. 8. (a) Engineering stress-strain curves of as-received and the weld material, (b) Yield Strength (YS), Ultimate Tensile Strength (UTS) and Elongation of as-received and weld material, (c and d) SEM micrographs of the tensile fracture surface of the weld material.

Table captions

Table 1. The chemical composition (wt%) of the experimental press-hardened steel

Table 2. Weight and chemical composition of various GA-coatings used in the present study

Table 1. The chemical composition (wt.%) of the experimental press-hardening steel

C	Mn	Si	P	S	Al	Cr	Ti	B	Fe
0.23	1.19	0.25	0.016	0.002	0.05	0.20	0.031	0.0030	Bal.

Table 2. Weight and chemical composition of various GA-coatings used in the present study

Coating	**Weight (g/m^2)**			**Chem. Comp. (wt%)**		
	Top	Bottom	Tot.	Fe	Al	Zn
100 g/m^2	49.7	50	99.7	12.7	0.28	Bal.
120 g/m^2	59.1	60.2	119.3	12.1	0.27	Bal.
140 g/m^2	69.8	71.1	140.9	13.5	0.30	Bal.

Research Highlights

- The laser-Zn plasma interaction results in higher energy dissipation and substantial dependence of the welding window on the GA-coating weight.
- A model has been established to interpret the correlation between heat input and penetration depth including a coating weight coefficient.
- EDX analysis confirmed a slight mixing of the GA-coating into the weld pool.
- A significant necking occurred before failure, suggesting that the joint is resistant to various concavity levels in different coating conditions.

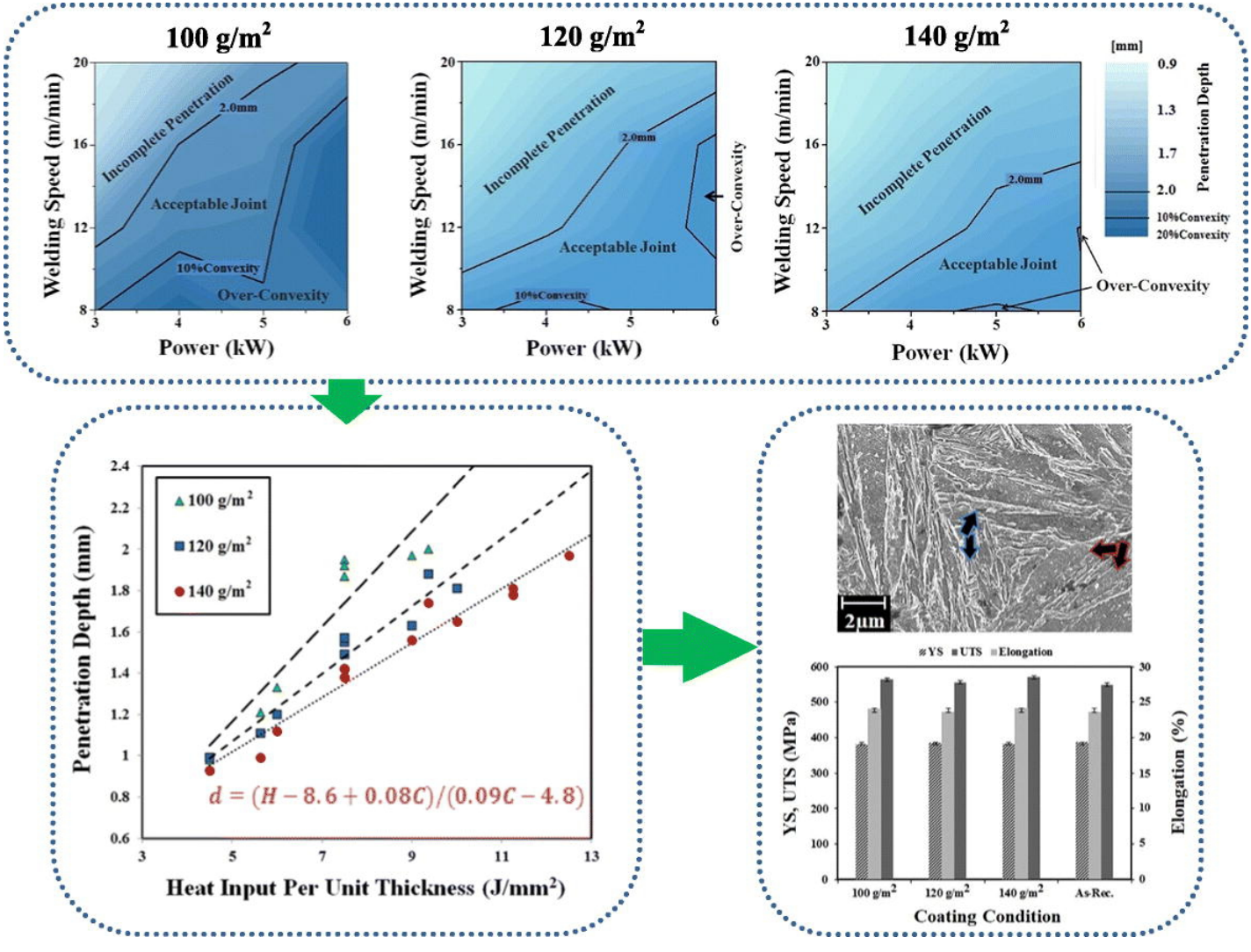

Graphics Abstract

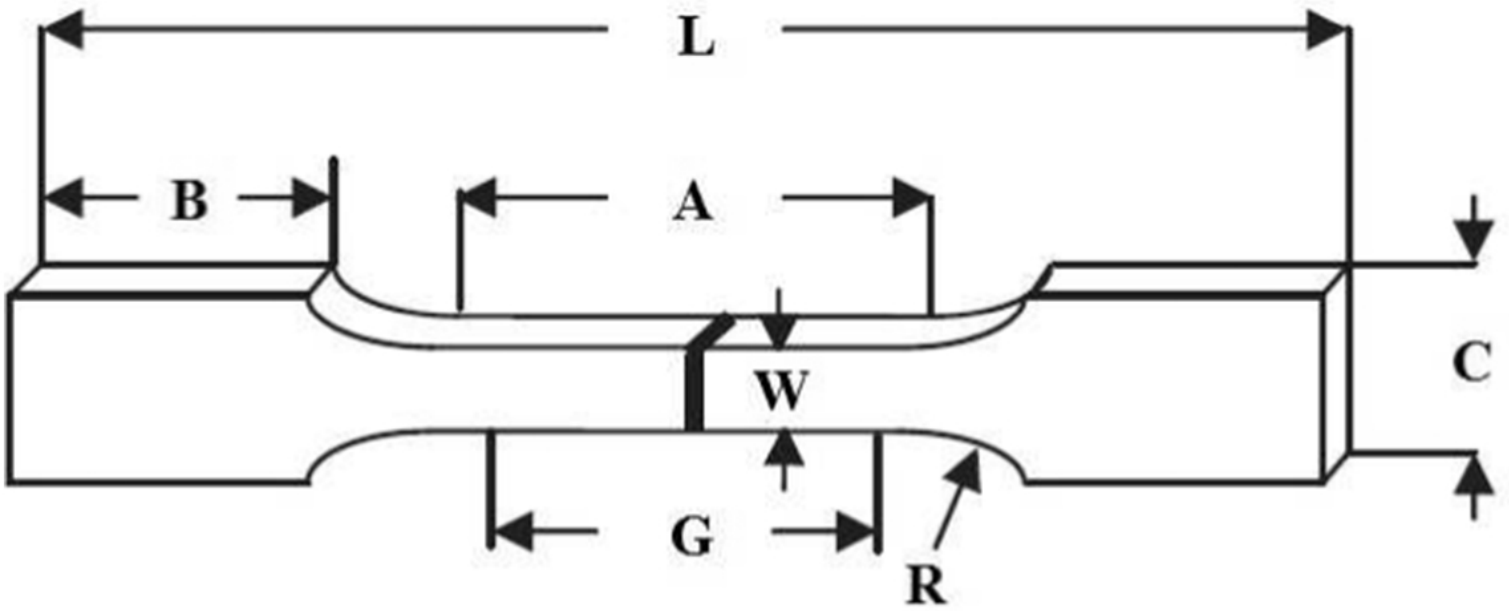

Dimension (mm)	
G	50
W	12.5
L	200
A	57
B	50
C	20
R	12.5

Figure 1

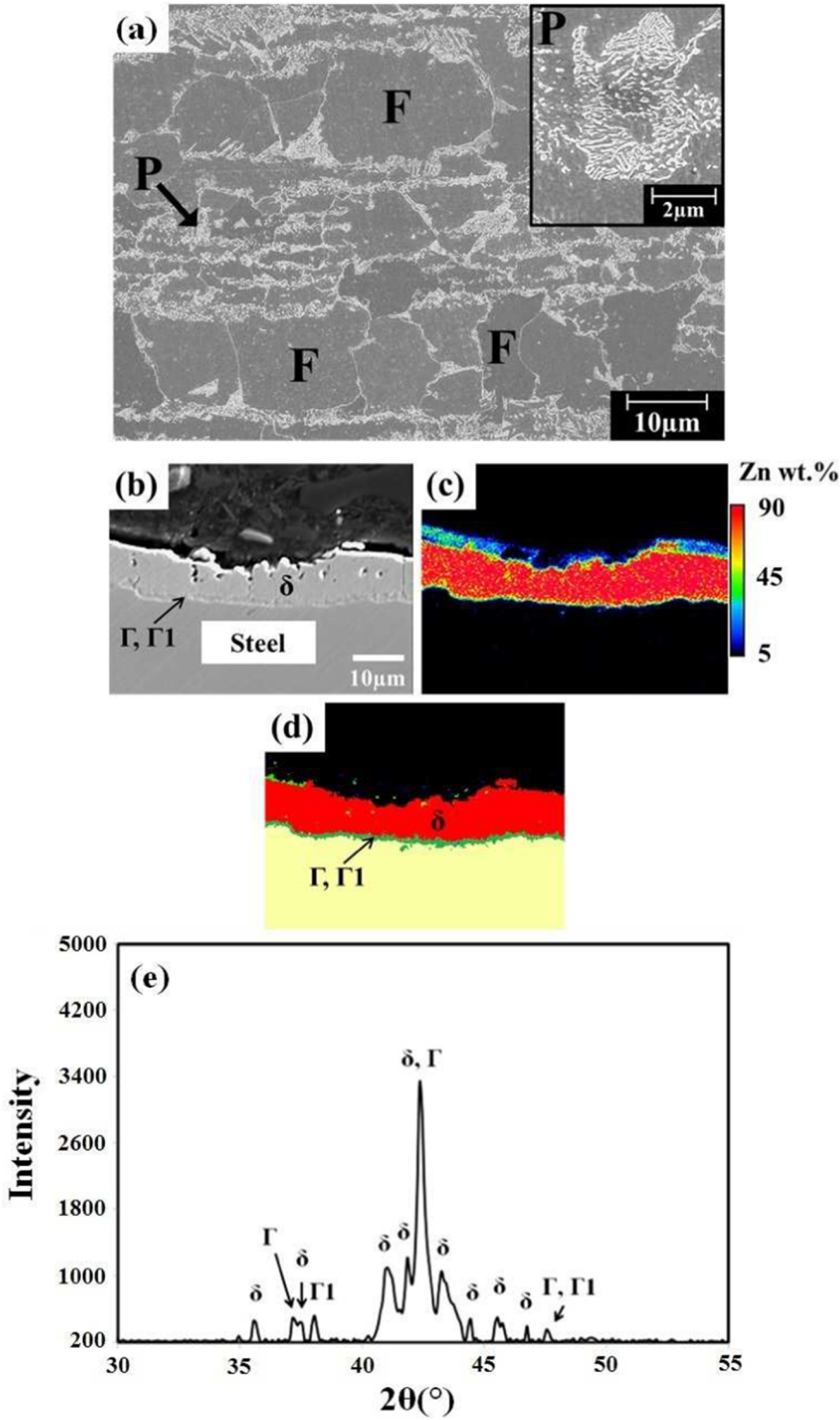
(a)
F
P
P
2μm
F
F
10μm
(b)
δ
Γ, Γ1
Steel
10μm
(c)
Zn wt.%
90
45
5
(d)
δ
Γ, Γ1
(e)
Intensity
5000
4200
3400
2600
1800
1000
200
δ, Γ
Γ
δ
δ
δ
δ
δ
Γ1
δ
δ
δ
Γ, Γ1
30
35
40
45
50
55
2θ(°)

Figure 2

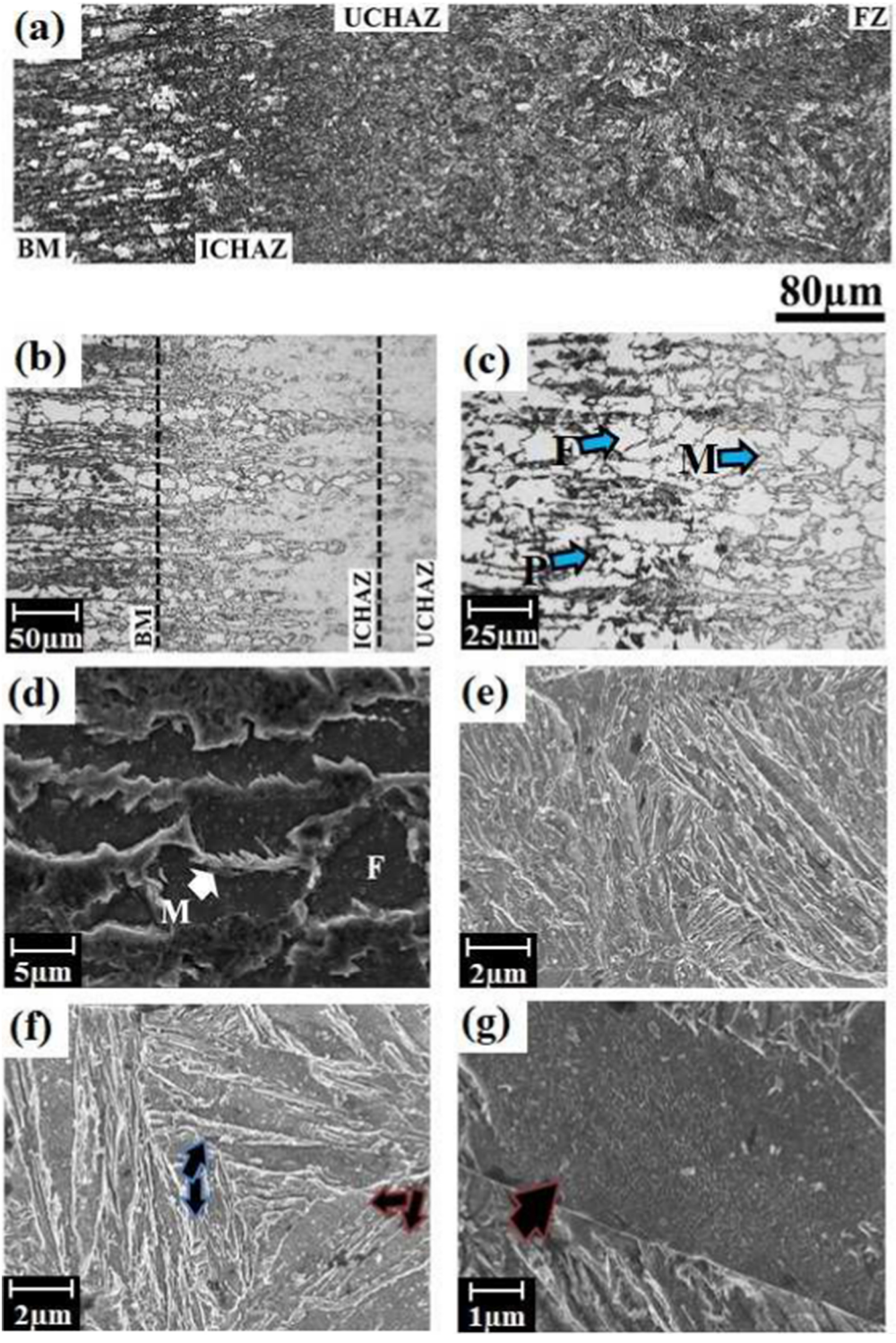
(a)
UCHAZ
FZ
BM
ICHAZ
80μm
(b)
50μm
BM
ICHAZ
UCHAZ
(c)
F
M
P
25μm
(d)
M
F
5μm
(e)
2μm
(f)
2μm
(g)
1μm

Figure 3

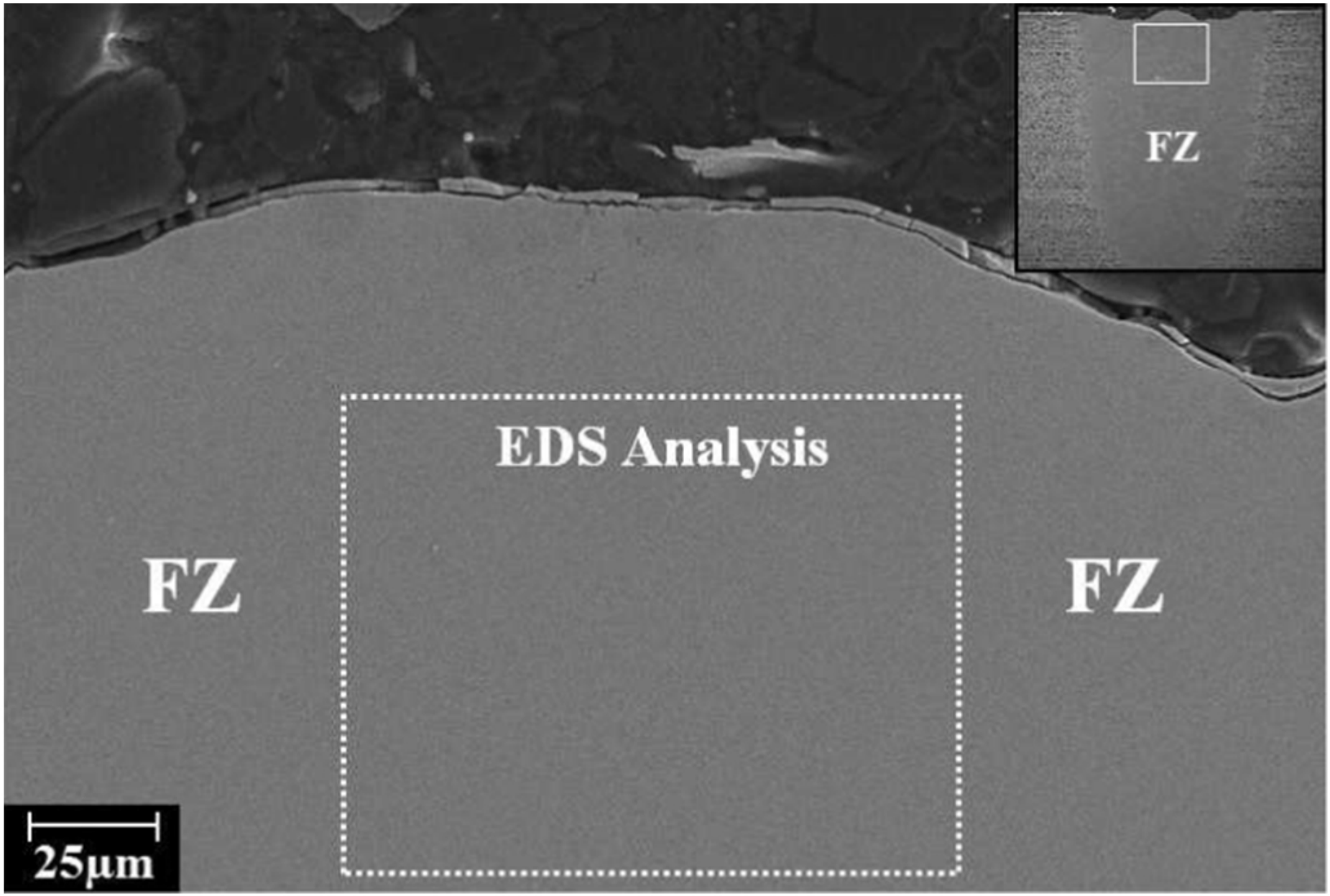

Figure 4

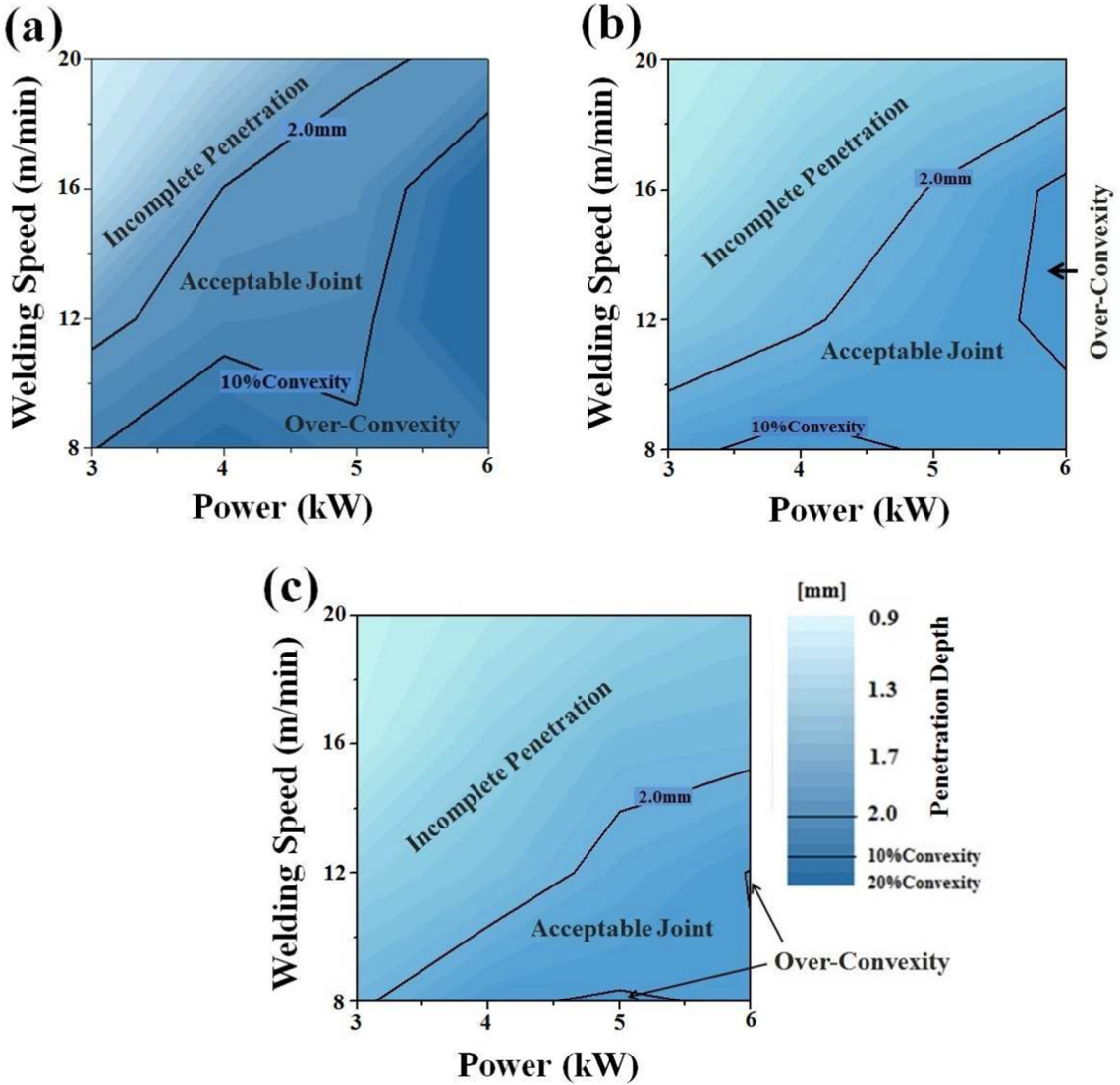
(a)
Welding Speed (m/min)
Power (kW)
Incomplete Penetration
2.0mm
Acceptable Joint
10%Convexity
Over-Convexity
(b)
Welding Speed (m/min)
Power (kW)
Incomplete Penetration
2.0mm
Acceptable Joint
10%Convexity
Over-Convexity
(c)
Welding Speed (m/min)
Power (kW)
Incomplete Penetration
2.0mm
Acceptable Joint
Over-Convexity
[mm]
0.9
1.3
1.7
2.0
10%Convexity
20%Convexity
Penetration Depth

Figure 5

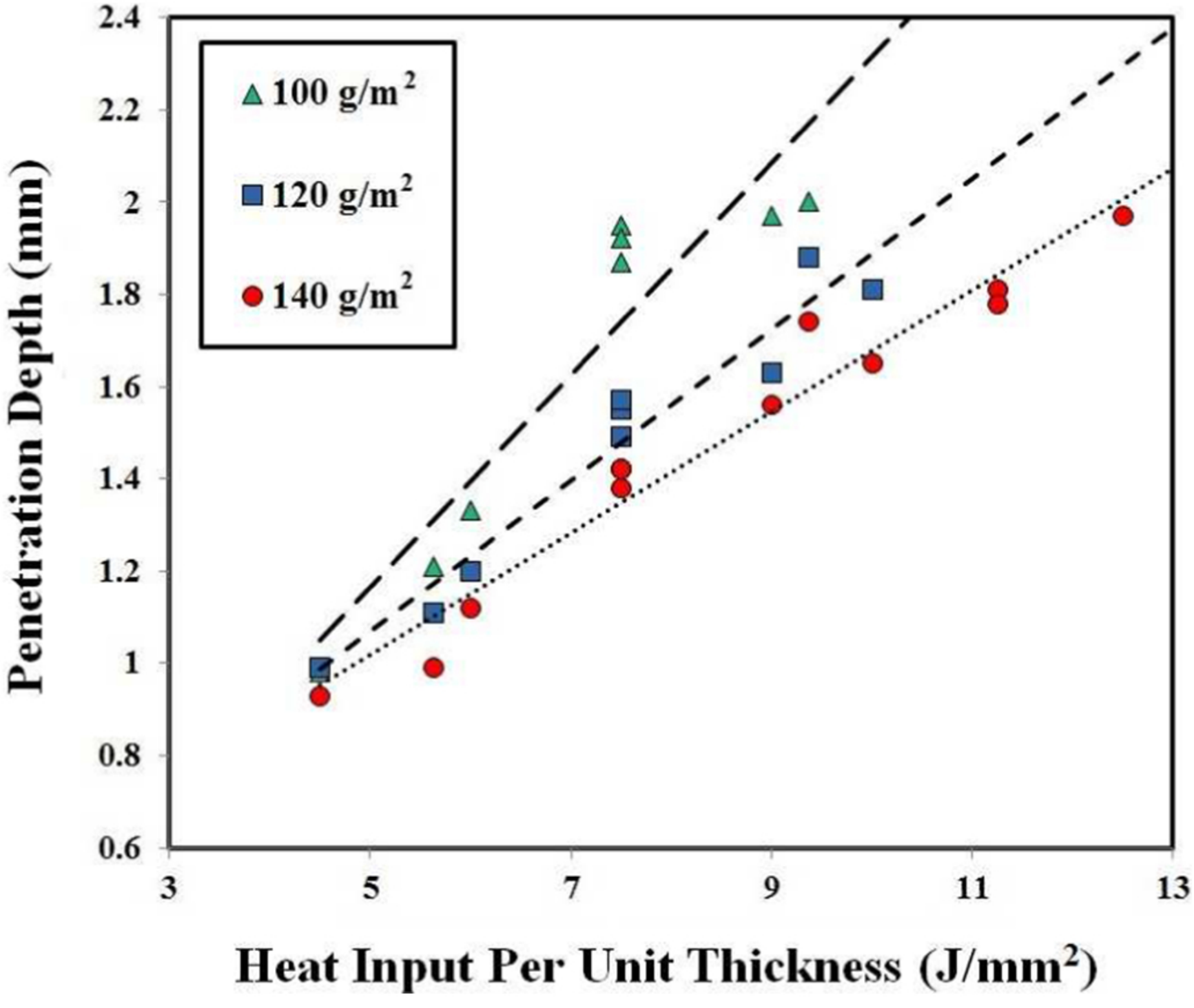
100 g/m²
120 g/m²
140 g/m²
Penetration Depth (mm)
2.4
2.2
2
1.8
1.6
1.4
1.2
1
0.8
0.6
3
5
7
9
11
13
Heat Input Per Unit Thickness (J/mm²)

Figure 6

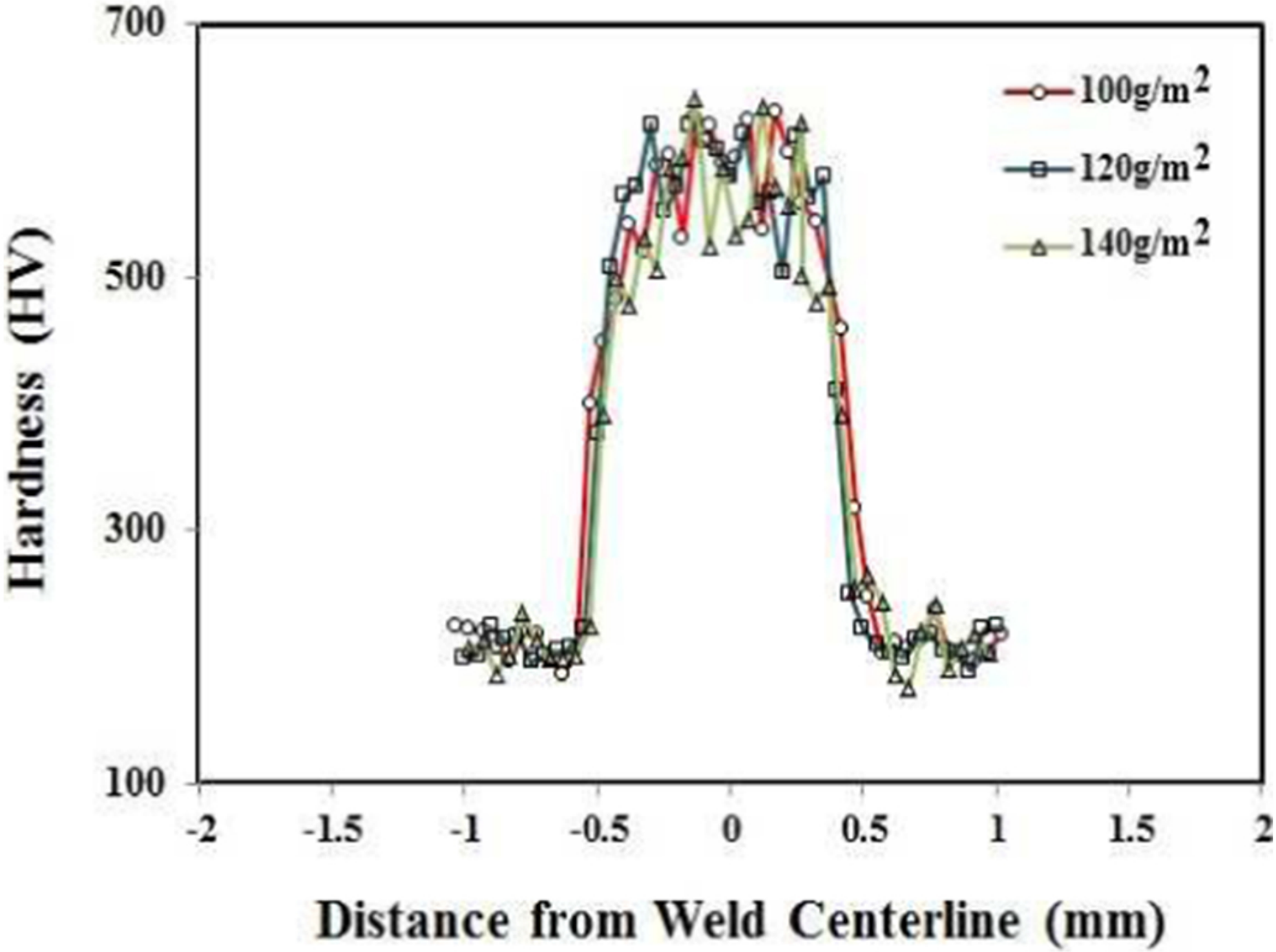
700
500
300
100
Hardness (HV)
100g/m2
120g/m2
140g/m2
-2
-1.5
-1
-0.5
0
0.5
1
1.5
2
Distance from Weld Centerline (mm)

Figure 7

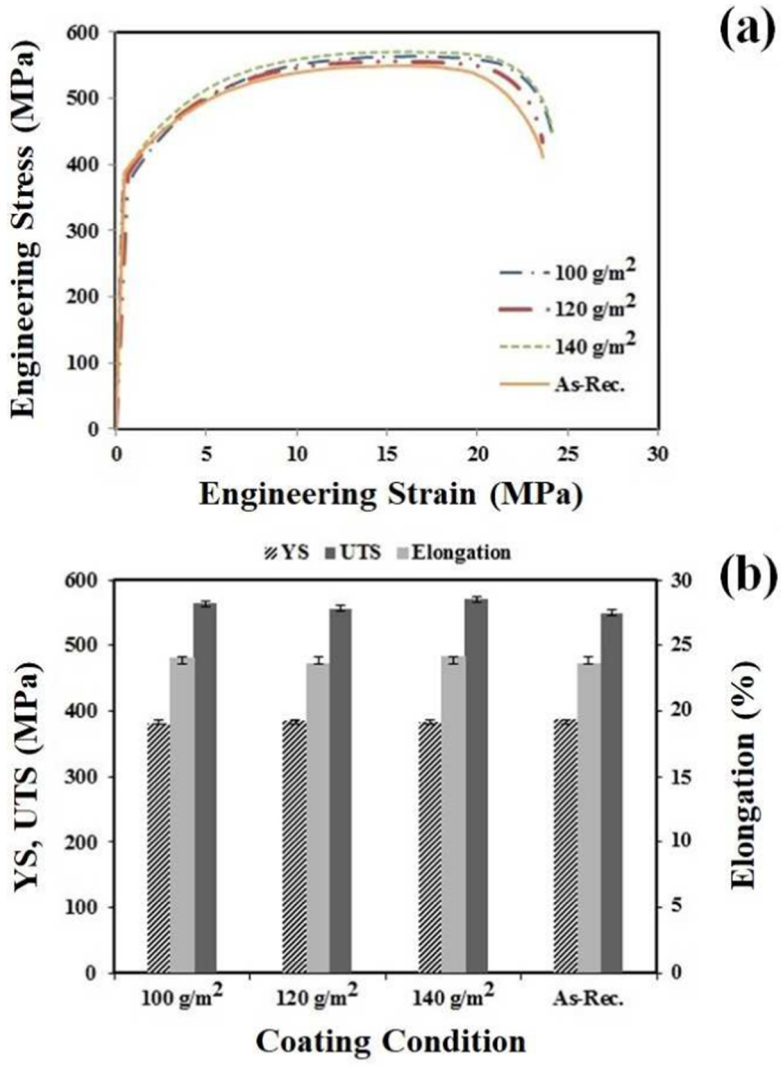
(a)
Engineering Stress (MPa)
Engineering Strain (MPa)
100 g/m2
120 g/m2
140 g/m2
As-Rec.
(b)
YS
UTS
Elongation
YS, UTS (MPa)
Elongation (%)
100 g/m2
120 g/m2
140 g/m2
As-Rec.
Coating Condition

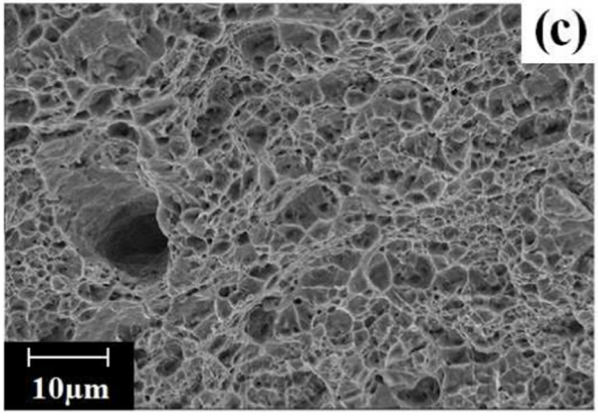
(c)
10μm

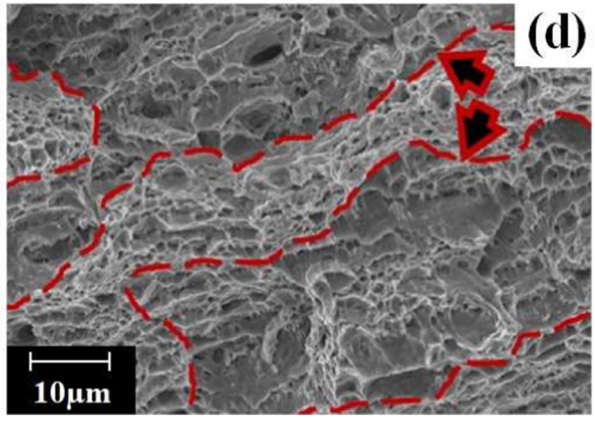
(d)
10μm

Figure 8